RADIO SCIENCE, VOL. 42, RS6003, doi:10.1029/2007RS003652, 2007



# Mapping the GPS multipath environment using the signal-to-noise ratio (SNR)

Andria Bilich[1] and Kristine M. Larson[2]

Received 1 March 2007; revised 2 August 2007; accepted 22 August 2007; published 28 November 2007.

[1] GPS multipath, where a signal arrives by more than one path, is a source of positioning error which cannot be easily neutralized. Better understanding of the multipath environment, i.e., the direction of and distance to reflecting objects, is important for multipath mitigation during the site construction phase as well as discerning the impact of multipath on positioning estimates for existing sites. This paper presents a tool called power spectral mapping that visually represents the multipath environment of a GPS site. This technique uses the spectral content (frequency and magnitude) of signal-to-noise ratio (SNR) time series to determine which satellites, and therefore which portions of the antenna environment, contribute significant multipath error and at what frequencies. Wavelet analysis is used to extract the time-varying frequency and magnitude content of various multipath constituents, and these data are projected onto a map representing the GPS antenna surroundings. Power spectral map examples from stations with very different multipath environments are presented. The maps are interpreted in terms of potential sources of multipath reflections, and how these multipath signals contribute to positioning error at each station is also assessed.

**Citation:** Bilich, A., and K. M. Larson (2007), Mapping the GPS multipath environment using the signal-to-noise ratio (SNR), *Radio Sci.*, *42*, RS6003, doi:10.1029/2007RS003652.

## 1. Introduction

[2] Multipath is defined as one or more signals arriving at the GPS antenna by indirect paths. Two main categories of multipath exist: diffuse and specular multipath. Diffuse multipath, where the GPS signal is incident on a rough surface and the reflected signal is scattered in multiple directions, is generally uncorrelated with time and noise-like in behavior [*Braasch*, 1996]. In contrast, specular multipath, where the GPS signal is reflected from a relatively smooth surface, results in systematic errors in both pseudorange and carrier phase measurements. These systematic errors can be substantial and may lead to range errors on the order of meters for the pseudorange and several centimeters for phase measurements [*Braasch*, 1996]. Since precise positioning software [e.g., *Hugentobler et al.*, 2001; *King and Bock*, 1997; *Zumberge et al.*, 1997a] assumes a direct path between satellite and receiver, i.e., multipath does not exist, the presence of multipath errors in the GPS observables ultimately leads to positioning errors. Multipath error will also influence other scientific products derived from GPS observables, including timing [*Ray and Senior*, 2003], water vapor products [*Braun et al.*, 2001], and seismic waves [*Larson et al.*, 2003]. Thus an understanding of the causes and magnitude of multipath errors is important.

[3] Recent GPS studies and applications motivate the need for improved multipath characterization techniques, as these studies and applications provide an increased appreciation for the temporal and spatial complexity of site-specific multipath environments. With the advent of high-rate applications [*Bock et al.*, 2004; *Larson et al.*, 2007], errors due to multipath which have been largely ignored for 24-hour position estimates are now of greater concern. For example, in high-rate positioning solutions measuring seismic waves, multipath phase errors can have amplitudes and frequencies similar to the signal of interest [*Larson et al.*, 2007]. A method to evaluate the multipath environment at different frequencies and with a sense of orientation is therefore of great value.

[4] Conventionally, assessments of multipath error involve computing the pseudorange multipath combinations, MP1 and MP2 [*Estey and Meertens*, 1999]. For example, the IGS (http://igscb.jpl.nasa.gov/) tracks mul-

[1]National Geodetic Survey, Boulder, Colorado, USA.
[2]Department of Aerospace Engineering Sciences, University of Colorado, Boulder, Colorado, USA.


0048-6604/07/2007RS003652$11.00

tipath statistics by computing these multipath observables for each site, computing a single RMS for the day, and comparing that value to the global network. This type of multipath measure has some drawbacks. First, summarizing multipath error with a single number for each day and station comes at the expense of a sense of multipath direction and magnitude differences. Another limitation of using MP1/MP2 is that it is also a measure of pseudorange precision. As reported by geodetic receivers, the pseudorange and thus MP1/MP2 observables are highly dependent on proprietary smoothing algorithms; therefore, inferring the carrier phase multipath environment from pseudorange data is inherently problematic. Large improvements in MP1/MP2 RMS more likely indicate changes in receiver firmware or antenna [*Ray and Senior*, 2003] than the actual multipath environment.

[5] Some methods already exist to capture the orientation and reflectivity of objects in the GPS multipath environment, but each comes with relative advantages and disadvantages. *Park et al.* [2004] built a directional antenna that could be used to precisely measure the orientation and magnitude of multipath effects, but this system has only been tested for the L1 frequency and requires reoccupation of the site if multipath conditions change. Similarly, ray tracing or modeling software [*Hannah et al.*, 1998; *Byun et al.*, 2002] is capable of depicting multipath directionality and magnitude when provided with precise measurements of all objects in the antenna environment; this kind of information is labor-intensive and rarely available in practice. Alternatively, several different types of time series can be derived from GPS observations and mapped to their respective satellite-receiver geometries, negating the need for on-site measurements. For example, GPS phase and pseudorange data can be linearly combined as in *Wanninger and May* [2001], but this method requires one or more multipath-free stations to form double differences. Mapping with the pseudorange multipath combination (MP1/MP2) [*Ogaja and Hedfors*, 2007; *Hilla*, 2004] allows analysis of a single station, but suffers from smoothing algorithms and pseudorange noise as described above. GPS data can be analyzed to yield solution postfit residuals [*Iwabuchi et al.*, 2004; *Morken et al.*, 2003; *Reichert*, 1999] for mapping purposes, but this requires a full positioning solution. In solving for position with least squares, multipath error will be distributed among estimated parameters (e.g., receiver clock and atmospheric delay) and the postfit residuals of other satellites in view, making it difficult to assign errors to a particular direction.

[6] This paper discusses a new technique for mapping the multipath environment at a GPS site that is distinct from most previous efforts in the following ways. First, we use signal to noise ratio (SNR) data rather than the phase or pseudorange observables. SNR is an observable commonly recorded by GPS receivers and easily reported in the RINEX format [*Gurtner*, 1994] that is sensitive to carrier phase multipath. By using SNR, we avoid positioning analysis, residuals, and the intrinsic redistribution of multipath error, and also avoid any need to double-difference. Additionally, dual-frequency receivers record SNR for both GPS frequencies (L1 and L2), allowing independent assessment of multipath effects on each frequency. SNR has been plotted on a satellite-by-satellite basis in previous studies (e.g., http://www-gpsg.mit.edu/~tah/snrprog), but we grid information derived from SNR (not the raw SNR themselves) to combine data from multiple satellites into a single picture. Secondly, the method described here is temporally dependent, in that SNR values from different days are inherently sensitive to changes in the multipath environment, unlike single-occupation calibration hardware or simulation software which assumes a static environment. Finally, this method evaluates multipath as a function of frequency, which in turn is related to the distance between the receiving antenna and the reflecting object. Physical parameters such as reflector distance and multipath amplitude will enable an analyst to evaluate the relative severity of multipath conditions and the objects responsible for these conditions, as is described below.

## 2. SNR and Phase Multipath

[7] Under the simplified model of GPS receiver response to tracking direct plus short-delay (less than 1.5 chips) reflected signals, carrier phase multipath is directly related to SNR. Long-delay multipath signals, where the reflected signal is delayed by greater than 0.1 miliseconds for C/A code and 0.01 milliseconds for P-code, will be rejected by the tracking algorithms. Derivations of the relationships between carrier phase error and SNR for short-delay multipath have been given by many others [*Georgiadou and Kleusberg*, 1988; *Comp and Axelrad*, 1997; *Reichert*, 1999; *Ray*, 2000; *Axelrad et al.*, 2005], but because these relationships are less well known outside of the engineering literature a brief derivation is provided. The below equations demonstrate that the frequency content of SNR data is directly related to the multipath environment, and with spectral analysis of SNR time series we can better understand the probable location of reflecting objects and severity of multipath errors resulting from these reflections.

[8] SNR data used in this study come from the S1 and S2 observables as reported in standard RINEX format [*Gurtner*, 1994]. The RINEX specification states that S1 and S2 observables are "raw signal strengths or SNR values as given by the receiver for the L1, L2 phase observations". Under this definition SNR and signal

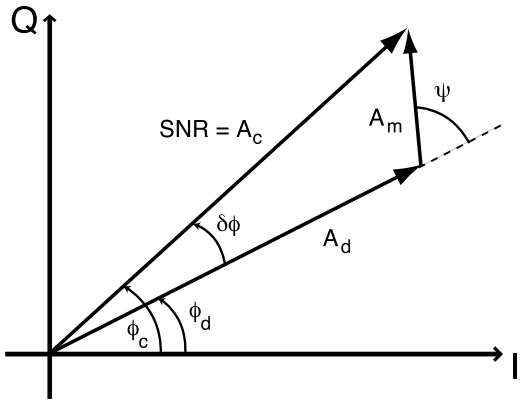


**Figure 1.** Phasor diagram describing carrier tracking loop operation and demonstrating the relationship between in-phase ($I$) and quadrature ($Q$) channels. Under multipath-free conditions, the loop will track the direct signal of amplitude $A_d$ and phase $\phi_d$. When a multipath signal (amplitude $A_m$) is introduced, the receiver instead records the composite signal ($A_c$) and its phase $\phi_c$. Tracking the composite signal biases the true phase $\phi_d$ by the phase error due to multipath, $\delta\phi$; the multipath relative phase $\psi$ represents the phase of the multipath phasor relative to the direct.

amplitude are terms that can be used interchangeably; assuming a constant level of noise, SNR is simply a scaled version of the signal amplitude or strength. In the following discussion, we predominantly use the term SNR to be consistent with other literature on this subject.

[9] In many GPS receivers, SNR is derived from the carrier tracking loop outputs. We represent the carrier tracking loop [*Ward*, 1996] in terms of a phasor diagram (Figure 1) that shows the phase relationship between the in-phase ($I$) and quadrature ($Q$) channels used in the carrier tracking loop. When no multipath is present, the phasor diagram would contain a single phasor of amplitude $A_d$; any misalignment of the local and incoming carriers results in a nonzero phase angle $\phi_d$, and the GPS carrier phase is measured by keeping track of $\phi_d$. The amplitude of the direct phasor is equivalent to the signal amplitude or reported SNR, $A_d = SNR$. When multipath is introduced, one or more additional phasors are added to the phasor diagram. The carrier tracking loop attempts to track a composite signal which is the vector sum of all phasors (direct plus multipath signal(s)); the SNR then becomes a measurement of composite signal amplitude, $SNR = A_c$. Using the law of cosines and geometric relationships expressed in the phasor diagram, composite SNR due to the direct signal plus one multipath reflection can be expressed as

$$SNR^2 \equiv A_c^2 = A_d^2 + A_m^2 + 2A_dA_m \cos\psi \qquad (1)$$

In this expression, SNR is a function of multipath amplitude $A_m$, direct amplitude $A_d$, and multipath relative phase $\psi$.

[10] Relating $\psi$ to physical characteristics of reflecting objects allows us to relate SNR to the environment surrounding the GPS antenna. We describe each reflecting object by its orientation (Figure 2), specifically the perpendicular distance between the antenna and the reflecting surface ($h$), the angle of reflection off of the surface ($\beta$), and the tilt of the surface relative to local level ($\gamma$). As shown by *Georgiadou and Kleusberg* [1988], the first two factors determine the path delay $\delta$, the additional distance traveled by an indirect (multipath) signal relative to the direct:

$$\delta = 2h \sin\beta \qquad (2)$$

Path delay is simply the spatial equivalent of multipath relative phase. By incorporating L1 or L2 GPS wavelength ($\lambda$) into this relationship, path delay is expressed in terms of the multipath relative phase. In addition, from the forward scattering geometry of Figure 2, note that $\gamma$ and $\beta$ are related to the satellite

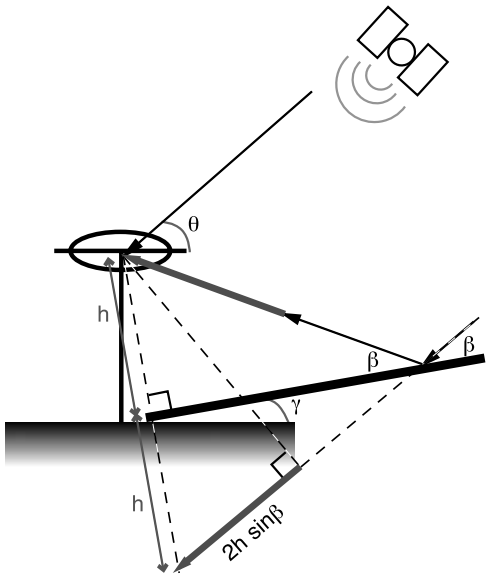


**Figure 2.** Geometry of a forward-scatter specular multipath reflection from a planar surface tilted at angle $\gamma$ relative to local level and located at a distance $h$ from the antenna phase center. The angle of incidence $\beta$ at the surface is equivalent to the angle of reflection, and $\theta$ is the satellite elevation angle. Bold arrows show the additional path length ($2h\sin\beta$) traveled by the multipath signal relative to the direct. All objects are considered coplanar (no third dimension).

elevation angle, i.e., $\theta = \beta + \gamma$. We more completely describe the reflector orientation by incorporating the tilt of the reflecting object $\gamma$ into equation (2):

$$\psi = \frac{2\pi}{\lambda}\delta = \frac{2\pi}{\lambda}2h\sin\beta$$
$$\psi = \frac{2\pi}{\lambda}2h\sin(\theta-\gamma) \quad (3)$$

Recognizing that the time-dependent behavior of SNR is dominated by the cosine of $\psi$ (equation (1)), we note that changes in SNR are related to the rate of change of $\psi$. By assuming persistent reflecting objects so that $\gamma$ is time-independent, we develop a term for the multipath frequency:

$$\frac{d\psi}{dt} = \frac{2\pi}{\lambda}2h\cos(\theta-\gamma)\frac{d\theta}{dt} \quad (4)$$

Satellite elevation angles are easily determined from GPS orbital information, so the $\theta$ and $d\theta/dt$ terms are known quantities. However, without knowledge of the GPS antenna's surroundings, the distance to and tilt of reflecting objects are both unknowns. If we assume all reflecting surfaces are horizontal (parallel to local level) at the point of reflection ($\gamma = 0^\circ$), the only unknown quantity in the multipath frequency equation is the distance to the reflecting object ($h$):

$$\frac{d\psi}{dt} = \frac{2\pi}{\lambda}2h\cos\theta\frac{d\theta}{dt} \quad (5)$$

Equation (5) is key to interpreting the maps we describe below. Slow oscillations in SNR (small $d\psi/dt$) will result from nearby objects, whereas fast or high-frequency oscillations in SNR (large $d\psi/dt$) are generated by reflections from distant objects. Equation (4) shows that tilted surfaces will yield slightly different $d\psi/dt$ than equation (5), so that if horizontal surfaces are incorrectly assumed, precise height determinations would be biased. However, in this study, the range of frequencies and possible heights studied in each power spectral map is far greater than any effect introduced by angled surfaces.

[11] Satellite motion substantially affects the period of multipath reflections due to the contributions of the $\cos\theta$ and $d\theta/dt$ terms in equation (5). When taking all satellites observed from a single station over the course of 24 hours, a large range of satellite elevations and rates of motion are possible. Consider a station at midlatitudes in the northern hemisphere, with some satellites passing directly overhead while others have short passes with small maximum elevations. For predominantly N–S satellite passes which reach high elevation angles, $\cos\theta$ approaches zero at the same time that $d\theta/dt$ becomes large. Conversely, satellites observed to the east and west will move more slowly (small $d\theta/dt$) and at lower elevation angles ($\cos\theta \approx 1$) than satellites passing overhead. How strongly these satellite motions drive multipath frequency depends on the distance to the reflecting object, $h$ – when $h$ is small, $\theta$ terms will dominate; with large $h$, $\cos\theta$ and $d\theta/dt$ terms are less dominant. Thus reflections from nearby objects may lead to a large range of expected multipath periods depending on the satellite, whereas multipath from distant reflectors will result in a tighter range of possible periods.

[12] Determining the location of reflecting objects is most relevant if we can also understand the magnitude of each object's contribution to positioning error. The carrier phase error due to multipath $\delta\phi$ contributes to positioning error, and is described by the phasor diagram (Figure 1). The phase error will be maximized when a multipath phasor is at right angles to the direct, i.e., multipath relative phase $\psi = 90^\circ$ or $270^\circ$. Therefore, the maximum possible phase error due to multipath (in radians) is only a function of the direct and multipath amplitudes:

$$\delta\phi_{\max} = \arctan\left(\frac{A_m}{A_d}\right) \quad (6)$$

Angular error is easily converted to an equivalent phase error in distance units when multiplied by $\lambda/2\pi$. Thus, determining multipath and direct signal amplitudes allows computation of the maximum possible phase error due to multipath.

## 3. Power Spectral Map Formation

[13] To summarize the relationships described above, the time-dependent behavior of SNR data has a direct relationship to the multipath environment - as the satellite moves through the sky, the reflection point of a multipath signal moves, changing the path delay (equation (2)) of the reflected signal relative to the direct and therefore the multipath relative phase (equation (3)). If the reflecting object's dimensions are sufficiently large, the multipath relative phase will rotate through one or more complete revolutions as the satellite moves and therefore the reflection point also moves across the object's surface. This motion creates a time-varying or oscillatory signature in SNR measurements.

[14] Therefore, given the assumption of reflectors whose orientation does not change over one or more multipath cycles, one can use localized estimates of SNR spectral power to effectively map the multipath environment. In the method described here, localized estimates of multipath frequency and amplitude are computed using the wavelet transform. Concentrating on a spectral band of interest, the wavelet power at every epoch is assigned to a satellite location (azimuth and elevation), then combined with spectral data from all available

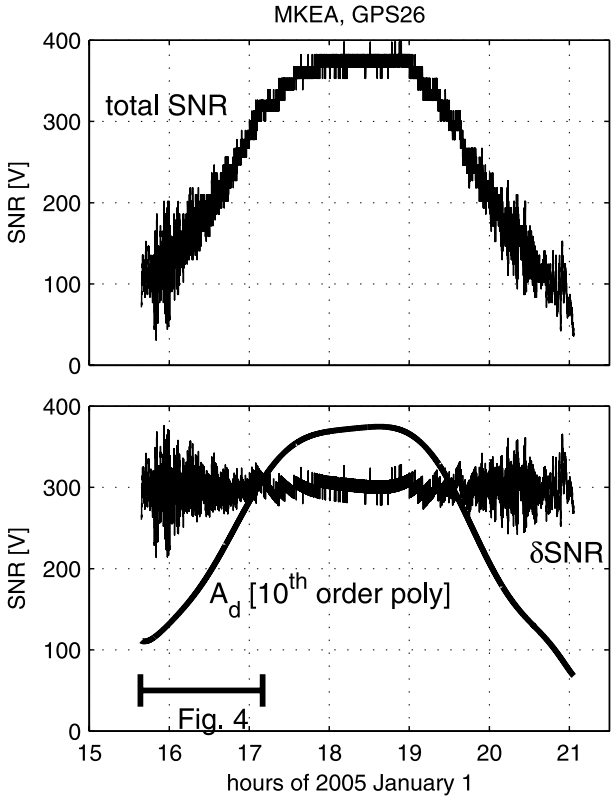


**Figure 3.** L1 SNR data as reported by the Ashtech Z-12 receiver and converted into V, station MKEA, 1 January 2005, GPS26. (top) Total SNR for both direct and multipath signals; (bottom) separation of direct ($A_d$) and multipath ($\delta SNR$) constituents for this satellite arc. The bracket marks the data section analyzed in Figure 4.

satellites and projected onto a sky plot which is a function of azimuth and elevation. This process forms a map depicting the multipath characteristics of a GPS site.

### 3.1. Data Selection and Preprocessing

[15] Since receiver manufacturers report SNR in a variety of units, SNR data from various receivers must first be converted into common units; we use voltage (V) so that the direct and multipath signals will be expressed in amplitude units. When plotted as an amplitude (Figure 3), we assume that the dominant trend in the time series is due to the direct signal ($A_d \gg A_m$) and multipath creates the smaller amplitude oscillations modulated on top of the $A_d$ trend. The best low order polynomial (order 3–15) is fit to and removed from the SNR time series; this polynomial fit is equivalent to $A_d(t)$ and leaves only $\delta SNR$, the SNR component due to multipath.

[16] We recognize that, in assuming that all long-period SNR contributions are due to the direct signal and not multipath, we are inherently concentrating on mapping multipath contributions from objects with larger $h$. That is, it is possible that multipath oscillations due to very close-in reflectors are mistakenly captured by the polynomial fit and separated from the SNR due to multipath. This separation of $A_d(t)$ and $A_m(t)$ is necessary for two reasons and cannot be omitted. First, the SNR time series must be zero mean for spectral analysis; by removing the direct signal contribution, the residual SNR time series $\delta SNR(t)$ will meet this criteria. Second, a measure of direct signal amplitude is necessary for computing maximum phase error (equation (6)). Incorrect assignment of part of the true $A_m(t)$ signal to $A_d(t)$ is less problematic than the converse; in this case, the $A_m/A_d$ ratio will decrease, leading to an underestimation of multipath error.

[17] After separating the direct and multipath contributions, each SNR multipath time series is padded using the method described in *Kijewski and Kareem* [2002]. Signal padding allows us to avoid loss of spectral information at the ends of the arc (where multipath effects will be most significant) due to edge effects. Each end of the original time series $\delta SNR(t)$ is padded with a negative, reversed order version of the same series. This type of signal padding places the signal of interest at the center of the series, away from edge effect corruption while locally preserving the frequency and bandwidth content of the signal.

### 3.2. Wavelet Analysis

[18] The wavelet analysis methodology and toolbox of *Torrence and Compo* [1998] was used to evaluate the frequency and power content of each $\delta SNR$ time series of length $N$ samples and sampling interval $\delta t$. We use the continuous wavelet transform $W_n$ where the series $\delta SNR$ is convolved with a scaled and translated version of the wavelet function, a function localized in time and space which has zero mean and is denoted by $\Psi$:

$$W_n(s) = \sum_{n'=0}^{N-1} \delta SNR_{n'} \Psi^* \left[ \frac{(n'-n)\delta t}{s} \right] \tag{7}$$

where the (*) denotes the complex conjugate. The wavelet transform is computed for a wavelet scale $s$ of interest, and this wavelet is translated along the time index $n$ to yield localized estimates of frequency and amplitude. In this study, the wavelet transform is computed over scales

$$s_j = s_0 2^{j\delta j}, \; j = 0, 1, \ldots, J$$
$$J = \delta j^{-1} \log_2 (N \delta t / s_0) \tag{8}$$

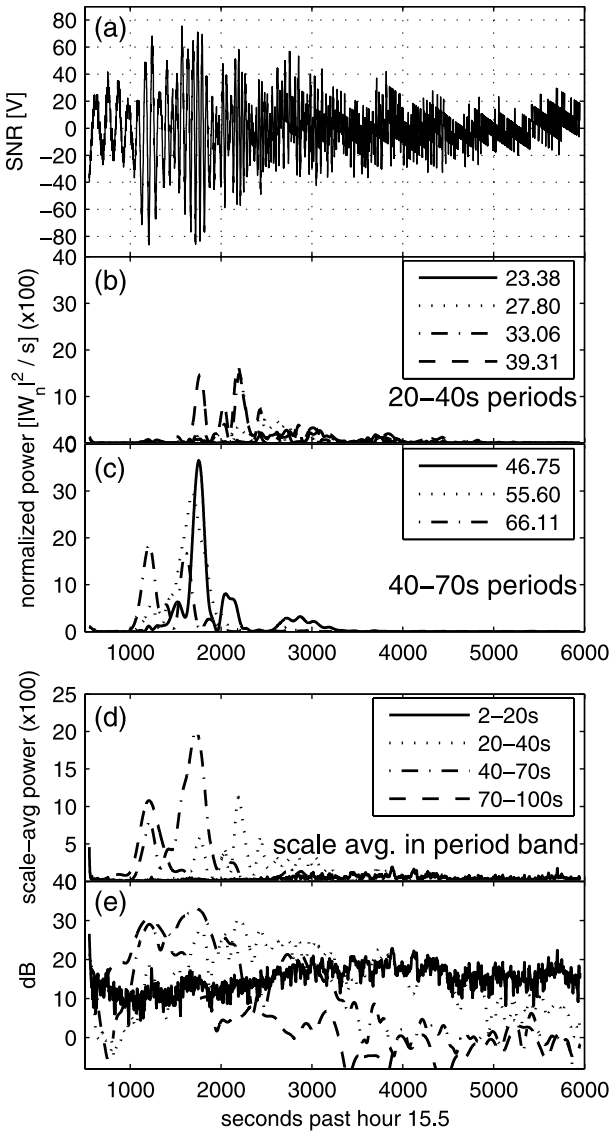


**Figure 4.** Example of wavelet analysis for the beginning of GPS26, MKEA, 1 January 2005. (a) $\delta SNR$ time series. (b) Wavelet power normalized by the wavelet scale ($|W_n(s)|^2/s$) for all scales $s$ falling in the 20–40 s period band; maximum power occurs around 2200 s. (c) Wavelet power for 40–70 s period band; maximum power now occurs around 1700 s. (d) Scale-averaged wavelet power ($\overline{W_n}^2$) for each period band of interest. (e) Same as Figure 4d, converted into dB (10*log10($\overline{W_n}^2$) to compress the range of values.

where $s_0 = 2\delta t$ is the smallest scale and $J$ is the largest, with spacing between scales of $\delta j = 0.15$. For computational efficiency, we approximate the continuous wavelet transform using the Fourier transform as outlined in *Torrence and Compo* [1998].

[19] Wavelet analysis provides better time-frequency localization than the windowed Fourier transform first used in power spectral map development [*Bilich*, 2006]. The wavelet transform is well suited for analysis of time series with nonstationary power at many different frequencies [*Daubechies*, 1990] as is the case with GPS multipath signals. The Morlet wavelet, a sinusoid modulated by a Gaussian, is used as the wavelet function $\Psi$ due to the simple relationship between wavelet scale and Fourier period [*Meyers et al.*, 1993], a desired numerical quantity. The Morlet wavelet is a complex wavelet; thus the wavelet transform of equation (7) is also complex.

[20] We extract two quantities of interest from each wavelet transform, multipath power and maximum phase error. For each scale $s$, multipath power can be expressed through the wavelet power spectrum, $|W_n(s)|^2$; the absolute value accounts for the complex nature of $W_n$. Wavelet analysis allows computation of spectral power over a range of possible wavelet scales or frequencies, yet power spectral maps can only be formed for one frequency at a time. To minimize the number of maps and simplify analysis, we examine multipath power in frequency bands of interest. Defining the limits of each frequency band in terms of the equivalent wavelet scales $s_x$ and $s_y$, we compute the scale-averaged wavelet power $\overline{W_n}^2$ for each band:

$$\overline{W_n}^2 = \frac{\delta j \delta t}{C_\delta} \sum_{j=x}^{y} \frac{\left|W_n(s_j)\right|^2}{s_j} \tag{9}$$

where $C_\delta$ is the reconstruction factor, equivalent to 0.776 for a Morlet wavelet [*Torrence and Compo*, 1998]. Figure 4 provides an example of banding and scale-averaging of wavelet power.

[21] Unlike multipath power, maximum phase error $\delta\phi_{\max}$ cannot be derived solely from the wavelet transform; it is a function of both multipath and direct signal amplitudes, i.e., $A_m$ and $A_d$, both expressed as a voltage. The composite amplitude of all multipath signals (in V) is equivalent to the wavelet amplitude or square-root of the scale-averaged wavelet power computed over all scales ($j = 0$–$J$):

$$A_m(t) = \sqrt{\overline{W_n}^2} = \frac{\delta j \delta t}{C_\delta} \sum_{j=0}^{J} \frac{\left|W_n(s_j)\right|^2}{s_j} \tag{10}$$

Recall that the direct amplitude $A_d(t)$ is equivalent to the polynomial fit to the original SNR data. Using these two

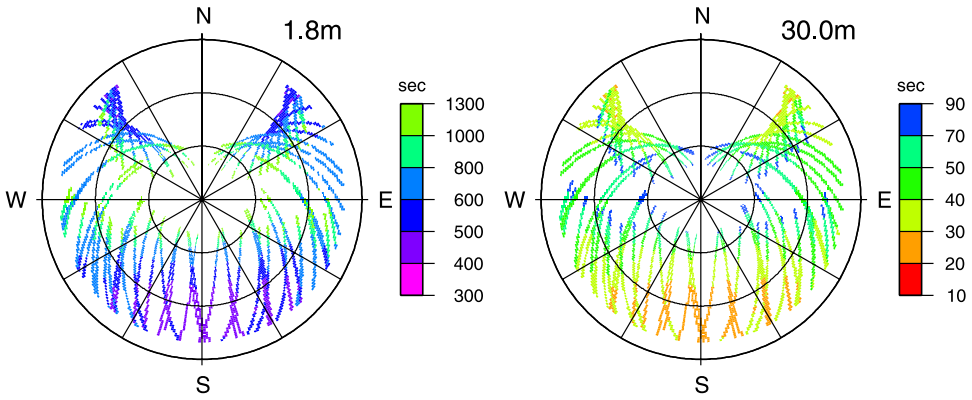


**Figure 5.** Forward model of expected periods for a horizontal reflecting surface (i.e., the ground) located at 1.8 m (left) and 30.0 m (right) below the antenna. Satellites in view from KYVW on 15 August 2005 were used for the simulation; the data were gridded by their mean in a 1 × 1 degree grid (no surface fit) to clearly display the satellite tracks where data are available. Note the change in scale (units of seconds) for the two plots.

quantities, equation (6) expresses the maximum possible phase error due to multipath as a function of time.

### 3.3. Gridding

[22] Finally, the quantity of interest (scale-averaged wavelet power or maximum phase error) for each satellite arc is combined with all other satellites in view into a single graphic. This is accomplished by considering each quantity not as a time-dependent function but as a spatial function of the satellite azimuth $\varphi$ and elevation $\theta$ at each epoch, i.e., $t \mapsto \varphi(t)$, $\theta(t)$. These data are projected onto an azimuth versus elevation grid which represents the sky above the GPS station being analyzed.

[23] The overlapping and sparse nature of GPS satellite tracks yields many data points in some parts of the sky and no data in others, leading to an incomplete picture of the multipath environment. To compensate for these effects, the composite data set is gridded and plotted using several Generic Mapping Tools modules [*Wessel and Smith*, 1998]. We take the mean of all values falling within a specified grid unit, then grid the data by solving for a surface under tension [*Smith and Wessel*, 1990] to create the final power spectral map. In the examples shown here, data are grouped using a $1^\circ\varphi \times 1^\circ\theta$ grid and the surface solution is bounded with tension factor of 0.4. It is possible to use other gridding methods (nearest neighbor, a strict block mean) and yield similar results; from comparisons we have made, the surface under tension yields the most complete and easy-to-understand power spectral maps possible. Note that gridding and plotting parameters (surface tension factor, grid size, etc.) can be altered to account for different data sample rates or multipath frequencies of interest, as appropriate.

### 3.4. Forward Model

[24] The spatial and temporal behavior of GPS satellite motions and their effect on power spectral maps is illustrated through simple forward modeling examples. We use satellites as viewed from KYVW, a station in southern California (33.9°N, 116.2°W), on 15 August 2005. With readily-available GPS orbital data, it is straightforward to determine each satellite's azimuth and elevation as a function of time, and consequently the rate of change in elevation $d\theta/dt$. These factors are used to model the expected multipath frequency (equation (5)) for a reflector at distance $h$ as a function of satellite position.

[25] Figure 5 presents the expected multipath periods for reflections from a single horizontal surface of infinite extent. These are not true power spectral maps, which display power contained within a specified frequency band. Instead, the plots in Figure 5 show which parts of the sky should yield high-power returns if one were to form power spectral maps for a particular frequency (period) band. These examples do not involve a surface fit to the available data, but instead employ only the block mean strategy to better reveal the variability in the ungridded multipath periods and represent the actual satellite locations.

[26] In the 1.8 m example (Figure 5a), the southern portion of the sky has systematic multipath periods of 400–500 s; periods lengthen to the east and west (500–800 s) and become rather large (>800 s) as each satellite approaches its apex. The same satellites observed at KYVW are also used to simulate reflections from a 30.0 m horizontal surface (Figure 5b). As demonstrated for this large $h$ value, the higher frequency multipath

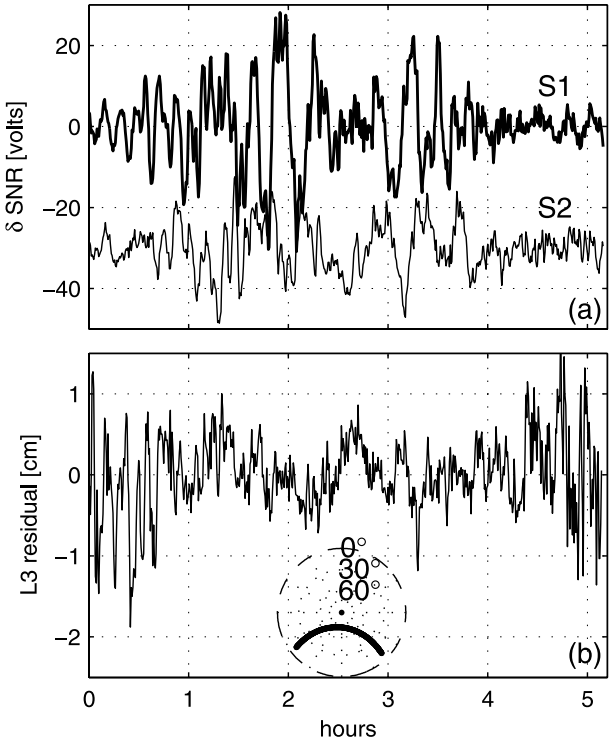


**Figure 6.** Data from PRN5, TRO1, 15 August 2005. (a) SNR values after direct signal has been removed from each GPS frequency; the S2 curve has been offset for clarity. (b) L3 PPP residuals. The inset sky plot shows the location of the satellite during the data segment shown; the satellite travels from west to east over the time period shown.

(with shorter periods) will be easier to distinguish on a power spectral map due to the decoupling of $d\psi/dt$ and $d\theta/dt$. These results are consistent with the above discussion on the influence of each term in equation (5), and provide information on what can be expected from power spectral maps in different frequency bands of interest.

## 4. Multipath Environment From Power Spectral Maps

[27] The application of this method is demonstrated using three continuous GPS sites from geodetic networks. The first, TRO1, is representative of sites situated on or near buildings. The second site, MKEA, shows multipath over a range of high frequencies consistent with reflections from distant topography. The final site, KYVW, has a composite multipath signature dominated by near-field ground multipath with sporadic far-field multipath related to local topography.

[28] To relate these multipath maps to errors in GPS positions, we compute solutions using the GIPSY software [*Lichten and Border*, 1987]. These solutions employ the ionosphere-free (L3) data combination, resulting in a combination of L1 and L2 multipath errors which emerge in the residuals for static positioning or in the positions for stochastic positioning. For the former case, the precise point positioning (PPP) strategy [*Zumberge et al.*, 1997a] is used to yield single-station postfit phase residuals. We implement PPP with 30 s satellite clocks [*Zumberge et al.*, 1997b] to yield 30 s residuals, and must decimate the phase and pseudorange data accordingly. For stochastic positioning, we compute high-rate (1-Hz) positions for the network described in *Larson et al.* [2007] and interpret the positions before any error mitigation stages such as modified sidereal filtering [*Choi et al.*, 2004] or stacking [*Wdowinski et al.*, 1997].

### 4.1. Tromsoe, Norway (TRO1)

[29] Station TRO1 operates an AOA ACT receiver with AOA chokering antenna at 30 sec sampling interval. The antenna is attached to a tall mast (4.09 meters) which is braced to the north side of a building; the antenna is ~1.3 meters above the building's roof, which is covered by tar paper and generally flat (Figure S1, available as auxiliary material).[1] We use this site to represent the multipath environment for GPS stations in urban settings, adjacent to buildings and other potentially reflective objects. As with many urban GPS stations, the location was likely chosen for access to power, requiring the antenna to be raised high above nearby structures for increased satellite visibility. Conventional wisdom dictates that this antenna configuration will minimize multipath affects because indirect signals from the supporting building enter the underside of the antenna gain pattern. However, the SNR data (Figure 6a) at this station clearly show very large amplitudes at periods consistent with a close reflector, i.e., the rooftop.

[30] Owing to the station's high latitude (69.6°N), the GPS satellites never achieve a very high elevation (most stay below 50°) and move very slowly; for example, the satellite pass displayed in Figure 6 takes over 5 hours. The slow rate of change with respect to elevation yields elongated multipath periods (equation (5)) compared to lower-latitude stations with similar multipath environments. Thus power spectral maps for this station must encompass a wide range of possible periods in order to adequately image the multipath environment. Figure 7 displays some power in the southern half of the sky over

[1] Auxiliary materials are available in the HTML. doi:10.1029/2007RS003652.

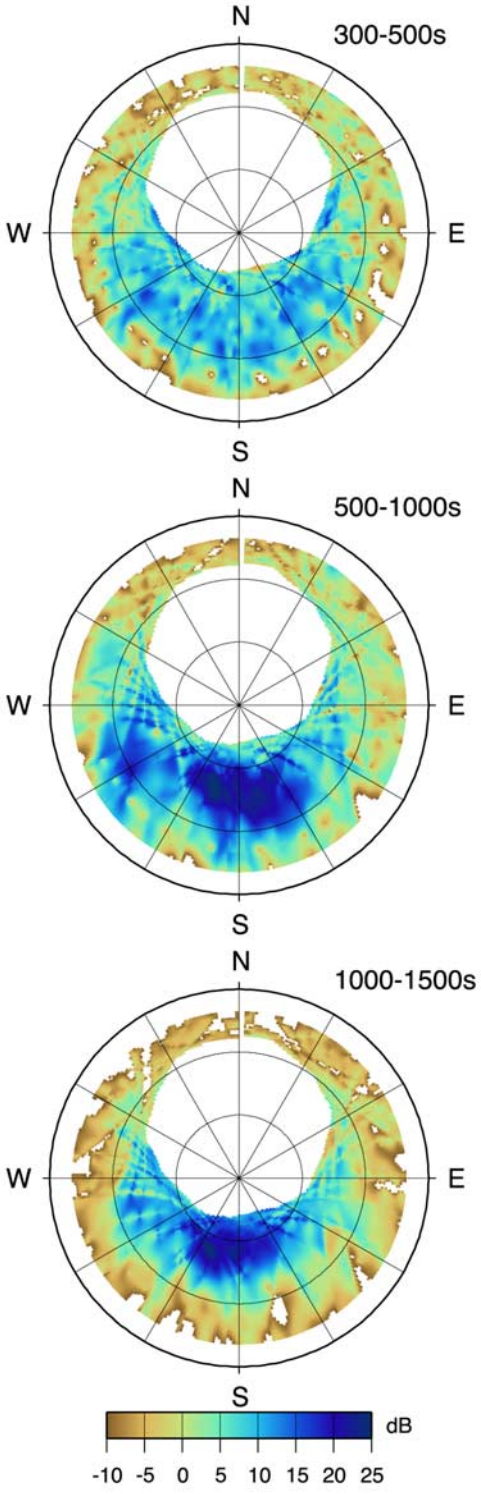


300–500 s periods; power increases sharply when considering 500–1000 s periods, with concentrations at midelevations to the south and southwest. At even longer periods (1000–1500 s), strong multipath power is observed only at the highest elevation angles to the south. These patterns are consistent with the slow motion of the GPS satellites as observed from TRO1 combined with a nearby reflecting object. The location of high power areas also matches the roof location; the building's sides are oriented approximately N–S and E–W with the roof to the south of the antenna.

[31] However, these strong multipath signals are not significant when considering their contributions to positioning error. Figure 6b shows moderate (0.5–2 cm) L3 residual errors at the lowest elevation angles, and no significant error where we observe the largest multipath power at the middle of the satellite pass (Figure 6a). Recall that the direct signal power $A_d$ increases with satellite elevation angle (Figure 3) and consequently deweights the influence of $A_m$ in creating phase errors. Thus, although the roof presents a strong multipath reflector, the reflected signals do not contribute appreciably to the observed errors at TRO1. If the reflections were generated from lower elevation angles, however, this would not be the case.

### 4.2. Mauna Kea Volcano, Hawaii (MKEA)

[32] Station MKEA operates an Ashtech Z-12 receiver sampling at 1 sec, with an AOA chokering antenna mounted on a ~1.2 m tall post which is situated over bare, rocky ground (Figure S2). Adjacent objects include a VLBI antenna (~50 m away to the east) and cinder cones to the NW and SSE (Figures S2 and S3). The main characteristics of the SNR data are multipath oscillations with periods ranging from a few seconds to a few minutes, with very large amplitude oscillations observed on a subset of satellites and occurring at 0–200 s periods (Figures 4a–4c). Reflections from horizontal ground ~1.2 m below the GPS antenna would have periods around 800 s at the ends of the satellite arcs, so a reflecting surface other than the ground below the GPS antenna is responsible for these high-amplitude, high-frequency oscillations.

[33] To image the environment, power spectral maps were formed for variable size bins (spanning 20–40 s) over 10–130 s periods (Figure 8). At the shortest periods (10–30 s), the highest power is observed for satellites at 30° elevation to the SSE. With slightly longer periods

**Figure 7.** Power spectral maps for TRO1, 15 August 2005, where the band of multipath periods examined is given in the upper right corner of each map. The wavelet transform was computed using 30 s SNR data.

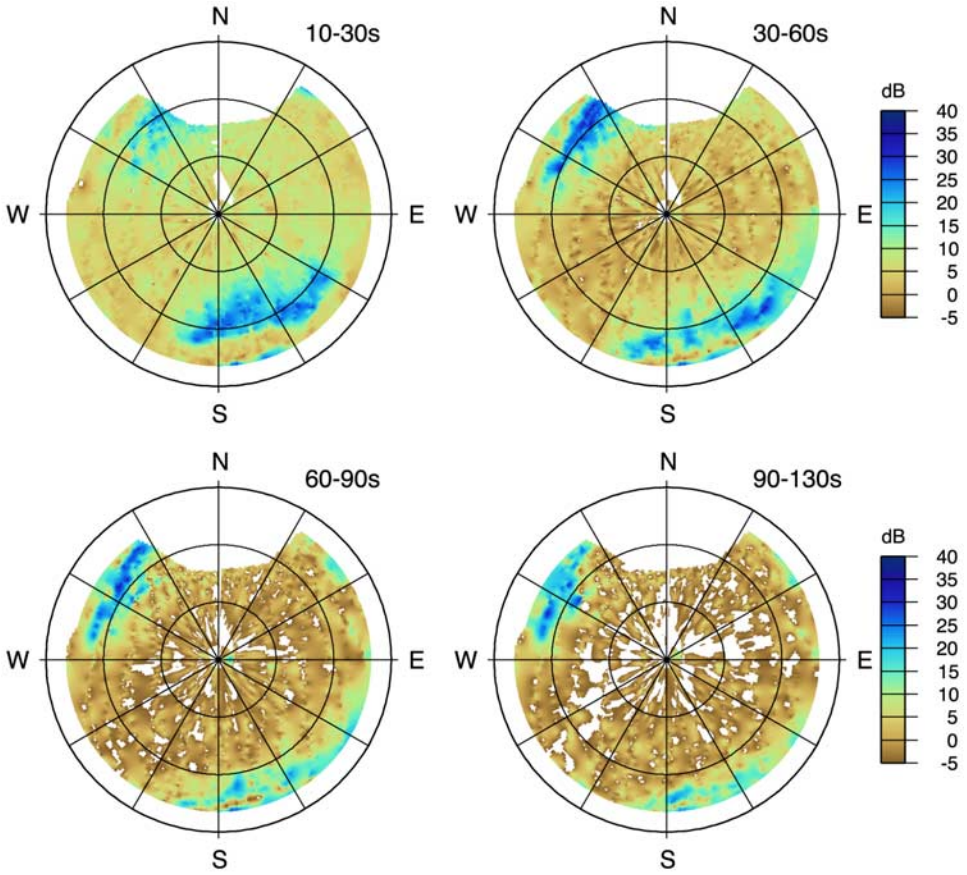


**Figure 8.** Power spectral maps for MKEA, 15 August 2005. The wavelet transform was computed using 1 s SNR data, then power estimates were downsampled to 5 s for gridding purposes.

(30–60 s and 60–90 s), the SSE feature moves to lower satellite elevation angles, and the highest power returns occur to the NW at approximately 30° elevation. The longest periods examined here (90–130 s) show spectral power concentrated at 10–15° elevation in the NW part of the sky.

[34] The observed patterns of high-magnitude multipath are consistent with the direction and orientation of the cinder cone flanks, and are approximated as a series of planar reflecting surfaces at varying tilt angles and antenna-reflector distances. Take PRN3 as observed from MKEA on 15 August 2005, a satellite that descends over the SSE cinder cone; over the last 4000 s of the observed descending pass, PRN3 travels from approximately 40°, 177° elevation and azimuth to 12.5°,169°. The L1 $\delta SNR$ data (Figure 9a) display high-power oscillations of ~20 s periods at the higher elevations which lengthen to ~120 s before the satellite disappears from view (Figure 9b); fitting a curve to these data yields the steep elevation angle versus period curve of Figure 9c. In Figure 9c, the heavy lines are a few example surfaces of infinite extent at antenna-reflector distance $h$ and reflector tilt $\gamma$. Note that no single planar surface, regardless of orientation or distance from the antenna, can explain the variation in multipath periods over the examined elevation range; it is not possible to simulate one steeply-inclined planar reflector that parallels the high-power trend of Figure 9b whose $\gamma$ does not exceed the satellite elevation angles (assuming forward-scatter geometry, the antenna could not receive reflections if $\gamma > \theta$). If we model the cinder cone as having a convex shape and break this shape into a series of small, localized planar reflectors with different $h$ and $\gamma$, a better fit to the multipath periods is achieved. Figure 9c presents sections of simulated multipath profiles for a series of surfaces which become more shallow and closer to the antenna as the satellite descends. These

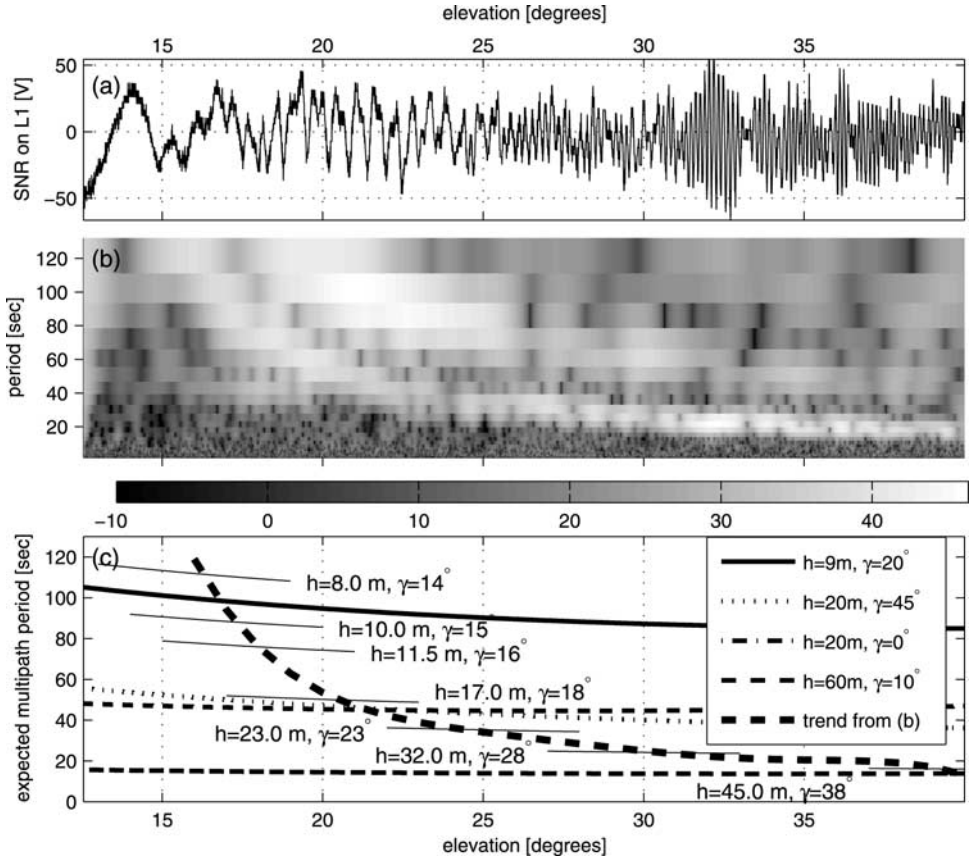


**Figure 9.** Analysis of the multipath periods contained in the final 12–40° of PRN3 as observed from MKEA on 15 August 2005, when the satellite descends over the SSE cinder cone (i.e., travels through 168–177° azimuth) over the course of ~4000 s. (a) L1 $\delta SNR$ data from PRN3 as a function of elevation angle. (b) Spectrogram of wavelet transform results, in dB of $V^2$/Hz; values below −10 dB have been excluded for clarity. (c) Expected multipath periods for a variety of planar surfaces at distance $h$ from the antenna, with inclination $\gamma$ relative to local level. The heaviest dashed line is a generalized trend of the persistent high-power reflection from Figure 9b. Note that no single surface (heavy lines), regardless of orientation or distance, can fit the trend of the high-power returns. The lightest lines are possible localized surfaces yielding a reflection angle of 2–3° at the elevation angle of intersection with the trend from Figure 9b.

possible surfaces were chosen to yield reflections at $\beta$ = 2–4° that geometrically intercept the GPS antenna, but a number of variations in inclination angle and distance are possible. Overall, convex surfaces consistent with the location and distance of the flanks of the cinder cones best describes multipath conditions at MKEA.

[35] These signals reflected from the cinder cones are of concern because they appear to be significant contributors to the unmodeled errors when computing the position of MKEA. As shown in Figure 10a, the multipath and direct signal amplitudes determined by the above analysis predict 5–20 mm of L1 phase error to the NW and SSE, the direction of the cinder cones. The 30 s L3 PPP residuals (Figure 10b) display the same patterns of high residuals and therefore positioning error. Thus, even though the area immediately surrounding the GPS antenna is free of multipath-generating objects, the cinder cones are responsible for a large part of the misfit at MKEA.

### 4.3. Keys View, Joshua Tree National Monument (KYVW)

[36] Station KYVW operates an Ashtech Z-12 receiver at 1-Hz with an Ashtech chokering antenna and SCIT radome. The deep drill-braced monument (Figure S4) used at KYVW is common in the SCIGN and PBO

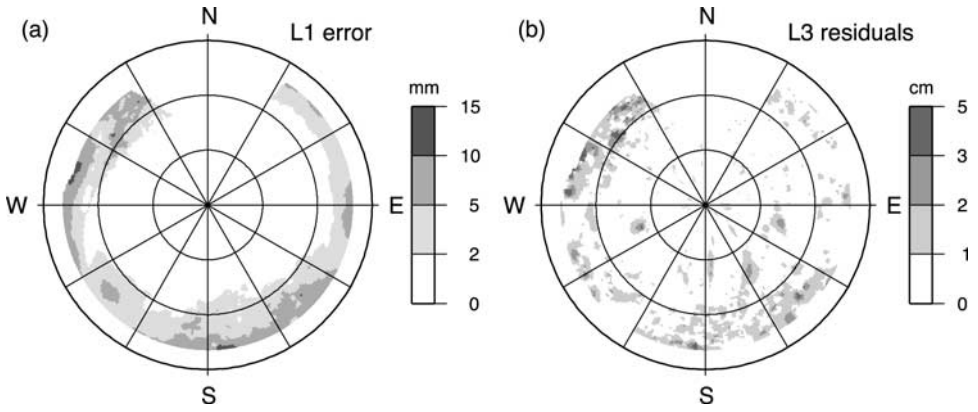


**Figure 10.** (a) Maximum L1 phase errors as predicted from SNR wavelet analysis versus (b) maximum L3 phase errors from PPP postfit residuals, station MKEA, 15 August 2005.

networks; although the height of this monument type varies for individual installations, a typical ground to antenna phase center distance is around 1.8 m (K. Austin, personal communication). The area surrounding the GPS antenna is scrub desert with gently-sloping hills to the NW and E (Figure S5). From site photos (http://www.scign.gallery2/v/KYVW), the monument is located in a sandy, flat-bottomed hollow.

[37] The dominant multipath signature is long period reflections (300–900 s) for satellite elevations of less than 30° (Figure 11a). These multipath periods are consistent with reflections from the ground immediately surrounding the antenna. The patterns of high spectral power are similar to the 1.8 m infinite reflector forward model of Figure 5: the shortest periods (300–450 s) to the south at low elevation angles, slightly longer periods (450–700 s) at midrange elevation angles and over a wider range of azimuths, and the longest periods (700–900 s) primarily to the east and west. Thus, SNR data from KYVW show a strong ground multipath signature consistent with a ground-antenna distance of approximately 1.8 m.

[38] A second high frequency signal is superimposed on the longer period oscillations for select satellites. When present, the multipath amplitudes of these signals are very small (1–5 V) in L1 data, but larger in the L2 SNR (Figure 12); we analyze the L2 SNR data to better reveal these small amplitude signals. These high frequency multipath signatures are present at 10–70 s periods (Figure 11b), and are very localized compared to the widespread near-field ground signature. These multipath periods correspond to distant reflecting objects: for example, using the motion of PRN6 while displaying these fast frequencies (Figure 12), the 30–50 s periods would correspond to 35–50 m distances. Given these approximate distances and direction to reflecting objects, we surmise that these signals are multipath reflections from the distant hillsides (Figure S5) much like the scenario described for MKEA.

[39] The influence of far reflectors on high-rate positioning precision is demonstrated by analyzing dual-frequency measurements from KYVW on 26 September 2004, two days before the $M = 6.0$ Parkfield earthquake; details regarding analysis of these 1-Hz data can be found in *Larson et al.* [2007]. Concentrating on the half hour after 8:03 UTC, at the same time that PRN16 rises above the 15° elevation cutoff imposed on this solution, the east component exhibits a brief section of ~30 s oscillations (Figure 13b). Looking at the L2 SNR time series for all satellites in view during this time period, PRN16 is the only satellite with similar frequency content (~40 s periods) (Figure 13a); all other satellites are in positions where the power spectral maps show no significant power at the frequencies observed in the east component. If PRN16 is removed from the solution, the 30 s oscillations are no longer present. This example demonstrates the importance of understanding and accounting for the multipath environment – had the Park-

**Figure 11.** Power spectral maps for KYVW, 26 September 2004 for L1 (a) and L2 (b) SNR, where the band of multipath periods examined is given in the upper right corner of each map. The wavelet transform was computed using 1 s SNR data, then power estimates were downsampled to 10 s (Figure 11a) or 5 s (Figure 11b) for averaging and gridding purposes. Note the change in data range between the two columns; values less than the scale minimum are omitted.

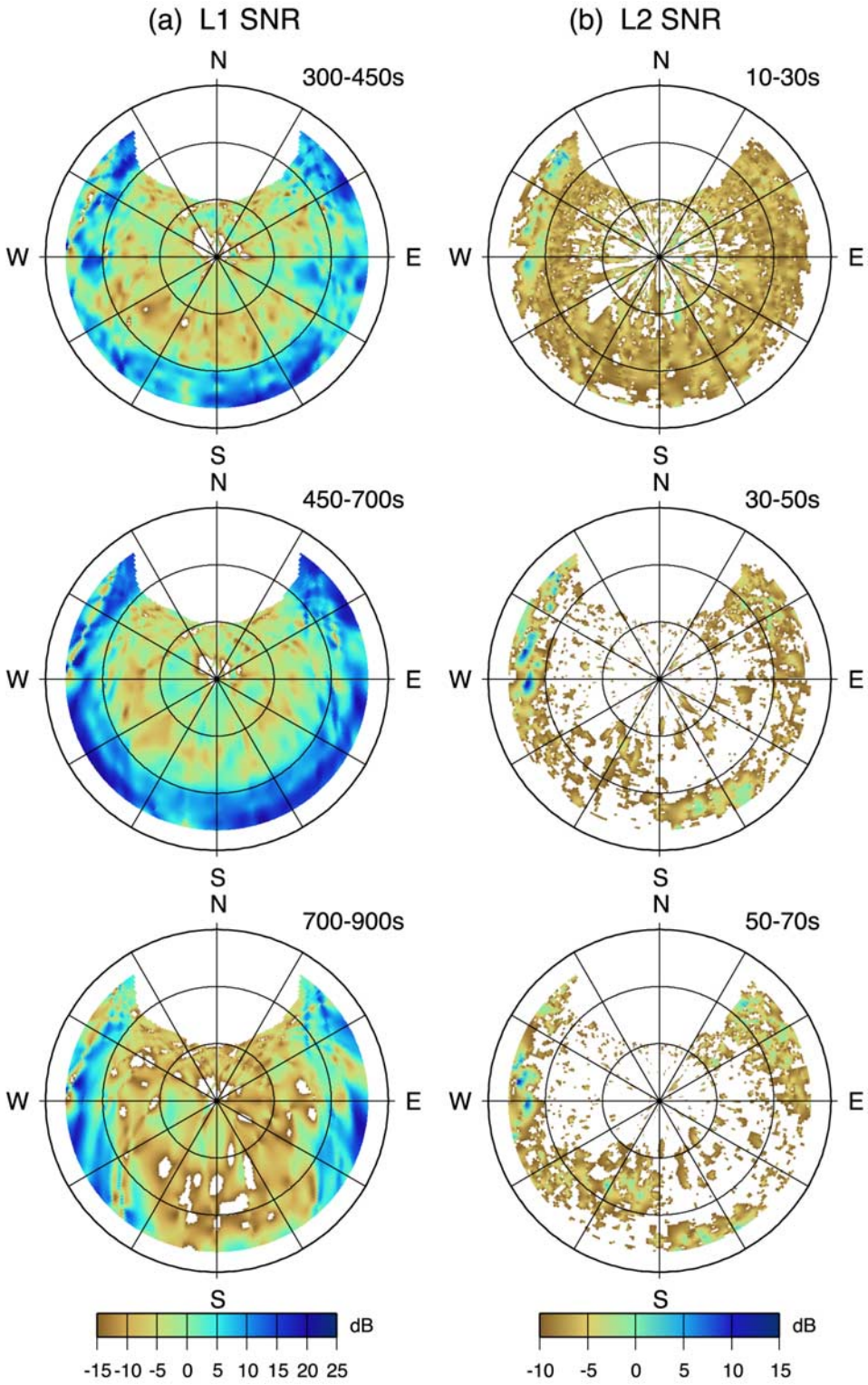
(a) L1 SNR
(b) L2 SNR
300-450s
10-30s
450-700s
30-50s
700-900s
50-70s
N
S
E
W
dB
-15 -10 -5 0 5 10 15 20 25
-10 -5 0 5 10 15

**Figure 11**

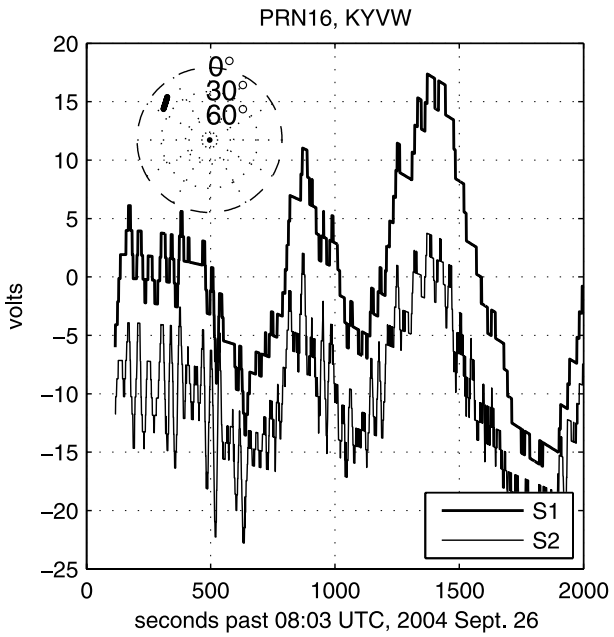


**Figure 12.** SNR values for PRN16, KYVW, 26 September 2004, after direct signal has been removed from each GPS frequency; the S2 curve has been offset by −10 V for clarity. The inset sky plot shows the location of the satellite during the data segment shown.

field earthquake occurred on this date, an analyst may have mistaken these oscillating multipath errors for seismic waves.

## 5. Conclusions

[40] A method has been developed to map the multipath environment using the SNR data reported by a GPS receiver. After removing the contribution of the direct signal, changes in the remaining SNR data are linked to phase multipath; we exploit this relationship to image the multipath environment. The wavelet transform is applied to SNR time series for each satellite in view to extract the time-varying amplitude and frequency content of each signal. By linking these time-varying characteristics to the GPS satellite position, this method produces spatially-varying amplitude or signal power estimates for different frequency bins. Frequency bears a direct relationship to the distance between the reflector and the GPS antenna, and binning the data by frequency allows formation of maps for different antenna-reflector distances. Thus we are able to interpret the multipath environment in terms of the distance to and reflectivity of objects surrounding a GPS site.

[41] SNR data have a variety of properties making them desirable for multipath analysis. SNR is sensitive to carrier phase multipath, and provides a data type to independently assess carrier phase errors on individual GPS frequencies without involving the carrier phase or pseudorange observables. The magnitude and frequency of SNR data will change with changes to the multipath environment, adding temporal as well as spatial resolution of multipath error. Finally, SNR is a quantity computed by all GPS receivers as a matter of routine; thus it is possible to form similar maps for any station where SNR data are available. These valuable SNR data are not always included in GPS data sets, however, so we encourage archivists to include SNR whenever possible.

[42] These maps demonstrate that multipath from topographic features may be more significant than previously believed. When choosing a site for GPS stations, sky blockages (buildings, hills, trees, etc.) are of primary concern, so GPS antennas are often situated at a large

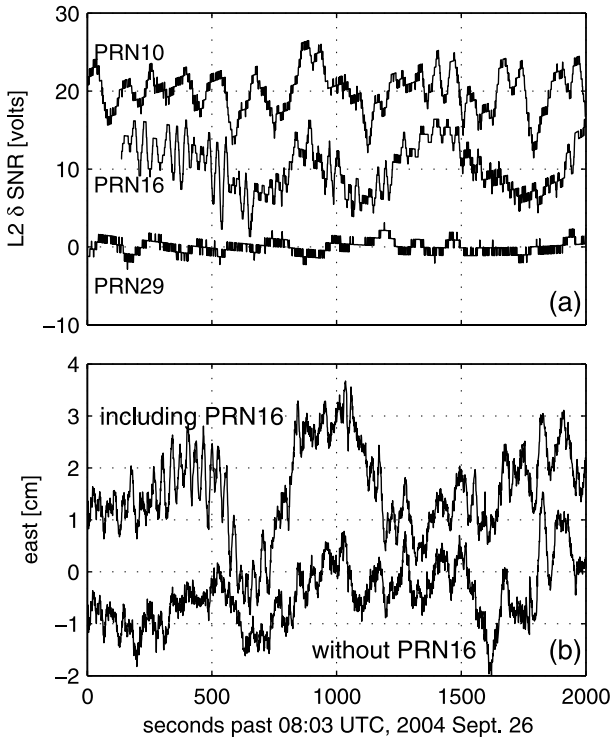


**Figure 13.** (a) L2 *δSNR* values and (b) east position for KYVW, 26 September 2004, the latter determined using dual-frequency observables. The three satellites in Figure 13a are indicative of the multipath signature of satellites in view from KYVW during this time period, with PRN16 exhibiting much faster and larger amplitude oscillations than all other satellites. East position computed with and without PRN16 is given in Figure 13b.

horizontal distance away from or vertical distance above potential blockages. Yet, if reflections from these distant objects are intercepted by the GPS antenna, they may result in high-frequency multipath errors in the GPS carrier phase. Thus, as the geodetic community increasingly uses high-rate GPS for applications such as seismology and volcano monitoring, multipath from even distant features and structures must be taken into account.

[43] Future work includes filtering the SNR time series before wavelet analysis to exclude frequencies of oscillation which are outside the range of periods sampled by the wavelet transform. The polynomial removal scheme implemented here is nonoptimal: when removing a polynomial of arbitrary order, it is possible that frequencies of interest are also removed from the time series while still failing to meet the zero-mean requirement of the wavelet transform. When reflections from close and far objects occur at the same time, the superposition of long and short period oscillations create difficulties for the wavelet transform – filtering to optimize for a particular frequency band would enable more accurate determination of amplitude and frequency. However, any filter applied to the SNR data must result in zero phase shift so that the relationship between satellite position and SNR oscillations is retained. Finally, the significance of the raw SNR observables must be better understood. Although not shown in this study, S1 and S2 data from some receiver models demonstrate data quality issues such as quantization or incorrect S1/S2 correlations which complicate power spectral map formation. A thorough study of SNR data quality for common geodetic receivers is warranted.

[44] **Acknowledgments.** The authors would like to thank Kevin Choi and the GMT user network for assistance with gridding and plotting methods, Penina Axelrad for valuable information about multipath and SNR data, Svein Ola Thorsen at the Norwegian Mapping Authority for providing site measurements of TRO1, and Asta Miklius at Hawaii Volcano Observatory for MKEA photographs. Suggestions from Giovianni Sella and an anonymous reviewer improved the manuscript. Wavelet software was provided by C. Torrence and G. Compo, and is available at URL http://paos.colorado.edu/research/wavelets/. We also thank SOPAC, JPL, IGS, CDDIS, NASA, and UNAVCO for infrastructure and archiving support. This research was sponsored by NSF grants on multipath (EAR-0003943) and high-rate GPS (EAR-0337206), and a NSF graduate student research fellowship (A.B.). All SCIGN (W. M. Keck Foundation, NASA, NSF, USGS, SCEC) data are in the public domain.

## References

Axelrad, P., K. M. Larson, and B. Jones (2005), Use of the correct satellite repeat period to characterize and reduce site-specific multipath errors, paper presented at ION GNSS, Inst. of Navig., Long Beach, Calif.

Bilich, A. (2006), Improving the precision and accuracy of geodetic GPS: Applications to multipath and seismology, Ph.D. dissertation, Univ. of Colo., Boulder.

Bock, Y., L. Prawirodirdjo, and T. I. Melbourne (2004), Detection of arbitrarily dynamic ground motions with a dense high-rate GPS network, *Geophys. Res. Lett.*, *31*, L06604, doi:10.1029/2003GL019150.

Braasch, M. S. (1996), Multipath effects, in *Global Positioning System: Theory and Applications*, vol. 1, edited by B. W. Parkinson et al., chap. 14, Am. Inst. of Aeronaut. and Astronaut., Reston, Va.

Braun, J., C. Rocken, and R. Ware (2001), Validation of line-of-sight water vapor measurements with GPS, *Radio Sci.*, *36*(3), 459–472.

Byun, S. H., G. A. Hajj, and L. E. Young (2002), Development and application of GPS signal multipath simulator, *Radio Sci.*, *37*(6), 1098, doi:10.1029/2001RS002549.

Choi, K., A. Bilich, K. M. Larson, and P. Axelrad (2004), Modified sidereal filtering: Implications for high-rate GPS positioning, *Geophys. Res. Lett.*, *31*, L22608, doi:10.1029/2004GL021621.

Comp, C., and P. Axelrad (1997), Adaptive SNR-based carrier phase multipath mitigation technique, *IEEE Trans. Aerosp. Electron. Syst.*, *34*(1), 264–276, doi:10.1109/7.640284.

Daubechies, I. (1990), The wavelet transform time-frequency localization and signal analysis, *IEEE Trans. Inf. Theory*, *36*, 961–1004.

Estey, L. H., and C. M. Meertens (1999), TEQC: The multi-purpose toolkit for GPS/GLONASS data, *GPS Solutions*, *3*(1), 42–49.

Georgiadou, Y., and A. Kleusberg (1988), On carrier signal multipath effects in relative GPS positioning, *Manuscr. Geod.*, *13*, 172–179.

Gurtner, W. (1994), RINEX: The Receiver-Independent Exchange Format, *GPS World*, *5*(7).

Hannah, B., R. Walker, and K. Kubik (1998), Towards a complete virtual multipath analysis tool, paper presented at ION GPS, Inst. of Navig., Nashville, Tenn.

Hilla, S. (2004), Plotting pseudorange multipath with respect to satellite azimuth and elevation, *GPS Solutions*, *8*, 44–48, doi:10.1007/s10291-004-0086-6.

Hugentobler, U., S. Schaer, and P. Fridez (2001), BERNESE GPS Software Version 4.2, Astronom. Inst., Univ. of Berne, Berne.

Iwabuchi, T., Y. Shoji, S. Shimada, and H. Nakamura (2004), Tsukuba GPS dense net campaign observations: Comparision of the stacking maps of post-fit phase residuals estimated from three software packages, *J. Meteorol. Soc. Jpn.*, *82*(1B), 315–330.

Kijewski, T., and A. Kareem (2002), On the presence of end effects and their melioration in wavelet-based analysis, *J. Sound Vibration*, *256*, 980–988, doi:10.1006/jsvi.2001.4227.

King, R. W., and Y. Bock (1997), Documentation for the GAMIT GPS analysis software, release 9.66, Mass. Inst. of Technol., Cambridge.

Larson, K., P. Bodin, and J. Gomberg (2003), Using 1 Hz GPS data to measure deformations caused by the Denali fault earthquake, *Science*, *300*, 1421–1424, doi:10.1126/science.1084531.

Larson, K. M., A. Bilich, and P. Axelrad (2007), Improving the precision of high-rate GPS, *J. Geophys. Res.*, *112*, B05422, doi:10.1029/2006JB004367.

Lichten, S., and J. Border (1987), Strategies for high-precision Global Positioning System orbit determination, *J. Geophys. Res.*, *92*, 12,751–12,762.

Meyers, S. D., B. G. Kelly, and J. J. O'Brien (1993), An introduction to wavelet analysis in oceanography and meteorology: With application to the dispersion of Yanai waves, *Mon. Weather Rev.*, *121*, 2858–2866, doi:10.1175/1520-0493.

Morken, D. M., B. J. Haines, and R. S. Nerem (2003), Utilizing site-specific antenna phase center calibration maps for reducing the noise in the GPS vertical, *Eos Trans. AGU*, *84*(46), Fall Meet. Suppl., Abstract F517.

Ogaja, C., and J. Hedfors (2007), TEQC multipath metrics in MATLAB, *GPS Solutions*, *11*(3), 215–222, doi:10.1007/s10291-006-0052-6.

Park, K. D., P. Elosegui, J. L. Davis, P. O. J. Jarlemark, B. E. Corey, A. E. Niell, J. E. Normandeau, C. E. Meertens, and V. A. Andreatta (2004), Development of an antenna and multipath calibration system for Global Positioning System sites, *Radio Sci.*, *39*, RS5002, doi:10.1029/2003RS002999.

Ray, J. K. (2000), Mitigation of GPS code and carrier phase multipath effects using a multi-antenna system, Ph.D. dissertation, Univ. of Calgary, Calgary, Alberta, Canada.

Ray, J., and K. Senior (2003), Geodetic techniques for time and frequency comparisons using GPS phase and code measurements, *Metrologia*, *40*, 215–232, doi:10.1088/0026-1394/42/4/005.

Reichert, A. K. (1999), Correction algorithms for GPS carrier phase multipath utilizing the signal-to-noise ratio and spatial correlation, Ph.D. dissertation, Univ. of Colo., Boulder.

Smith, W. H. F., and P. Wessel (1990), Gridding with continuous curvature splines in tension, *Geophysics*, *55*, 293–305.

Torrence, C., and G. P. Compo (1998), A practical guide to wavelet analysis, *Bull. Am. Meteorol. Soc.*, *79*, doi:10.1175/1520-0477.

Wanninger, L., and M. May (2001), Carrier-phase multipath calibration of GPS reference stations, *Navigation*, *48*(2), 113–124.

Ward, P. (1996), Satellite signal acquisition and tracking, in *Understanding GPS: Principles and Applications*, edited by E. D. Kaplan, Artech House, Norwood, Mass.

Wdowinski, S., Y. Bock, J. Zhang, P. Fang, and J. Genrich (1997), Southern California Permanent GPS Geodetic Array: Spatial filtering of daily positions for estimating coseismic and postseismic displacements induced by the 1992 Landers earthquake, *J. Geophys. Res.*, *102*, 18,057–18,070.

Wessel, P., and W. H. F. Smith (1998), New, improved version of Generic Mapping Tools released, *Eos Trans. AGU*, *79*(47), 579.

Zumberge, J., M. Heflin, D. Jefferson, M. Watkins, and F. Webb (1997a), Precise point positioning for the efficient and robust analysis of GPS data from large networks, *J. Geophys. Res.*, *102*, 5005–5018.

Zumberge, J. F., M. M. Watkins, and F. H. Webb (1997b), Characteristics and applications of precise GPS clock solutions every 30 seconds, *Navigation*, *44*(4), 449–456.

A. Bilich, National Geodetic Survey, 325 Broadway E/GC2, Boulder, CO 80305, USA. (andria.bilich@noaa.gov)

K. M. Larson, Department of Aerospace Engineering Sciences, University of Colorado, UCB 429, Boulder, CO 80309-0429, USA.